Journal of Solid State Chemistry 183 (2010) 1595–1603

Contents lists available at ScienceDirect

Journal of Solid State Chemistry

journal homepage: www.elsevier.com/locate/jssc

Single-crystal micro/nanostructures and thin films of lamellar molybdenum oxide by solid-state pyrolysis of organometallic derivatives of a cyclotriphosphazene

Carlos Díaz [a], Vladimir Lavayen [b], Colm O'Dwyer [c,*]

[a] Departamento de Química, Facultad de Ciencias, Universidad de Chile, Casilla 653, Santiago, Chile
[b] Departamento de Física, Universidad Técnica Federico Santa María, Valparaíso 2390123, Chile
[c] Department of Physics and Materials & Surface Science Institute, University of Limerick, Limerick, Ireland

ARTICLE INFO

Article history:
Received 11 November 2009
Received in revised form
27 April 2010
Accepted 7 May 2010
Available online 15 May 2010

Keywords:
Nanostructures
Metal oxides
Organometallic synthesis
Pyrolysis
Battery materials
Intercalation

ABSTRACT

The solid-state pyrolysis of organometallic derivatives of a cyclotriphosphazene is demonstrated to be a new, simple and versatile solid-state templating method for obtaining single-crystal micro- and nanocrystals of transition and valve metal oxides. The technique, when applied to Mo-containing organometallics $N_3P_3[OC_6H_4CH_2CN \cdot Mo(CO)_5]_6$ and $N_3P_3[OC_6H_4CH_2CN \cdot Mo(CO)_4\ py]_6$, results in stand-alone and surface-deposited lamellar MoO_3 single crystals, as determined by electron and atomic force microscopies and X-ray diffraction. The size and morphology of the resulting crystals can be tuned by the composition of the precursor. X-ray photoelectron and infrared spectroscopies indicate that the deposition of highly lamellar MoO_3 directly on an oxidized (400 nm SiO_2) surface or (100) single-crystal silicon surfaces yields a layered uniphasic single-crystal film formed by cluster diffusion on the surface during pyrolysis of the metal-carbonyl derivatives. For MoO_3 in its layered form, this provides a new route to an important intercalation material for high energy density battery materials.

1. Introduction

The method of solid-state pyrolysis of organophosphazene/organometallic as a synthetic templating method represents a new approach to the realization of micro- and nanocrystals of transition and valve metals and their respective oxides. Of these, MoO_3 is an extremely versatile material from many standpoints [1]. This material exhibits useful properties that have already been applied to sensing, electrochromic coating materials, layered host materials for solid-state thin film battery cathodes [2,3], solid-state lubricants [4] exhibiting load-independent friction [5], and even superconductivity [6] and thermoelectrics [7]. A recent review [8] has poignantly highlighted the importance of micro- and nanostructured MoO_3 and related sub-stoichiometric molybdenum oxides for charge storage/intercalation and particularly for electrochromics, properties that have been studied for a wide range of disordered partially crystalline or polycrystalline materials including amorphous MoO_3 films. Only brief studies of nanocrystalline MoO_3 materials for electrochromic applications have been reported to date [9] limited by the availability of single-crystal MoO_3 synthesis with size and crystal structure control and suitable surface deposition methodologies.

The recent interest in oxides, and in particular nano-oxides [10], as anodes for HEV lithium batteries is driven by the desire for an anode with a slightly more positive insertion voltage with respect to Li^+/Li to minimize any risks of high-surface-area Li plating while charging at high rates. Thus the ideal negative electrode for forthcoming vehicular applications that operate at higher potential than graphite are currently being investigated for future anode technologies [11]. MoO_3 and methods for high yield and purity are under renewed scrutiny since it (and other transition metal oxides) [12,13] operates at higher potentials relative to Li^+/Li during intercalation/insertion reactions. The Li^+ intercalation cycling properties of α-MoO_3 is proposed to be markedly improved upon nanostructuring, by minimizing the stability-reducing effect caused by the unit cell volume increases during intercalation [13]. The orthorhombic structure of α-MoO_3 is characterized by narrow channels of $\sim$2 nm. Intercalation of lithium ions into a crystal of this form would be aided if lithium ions can preferentially penetrate spaces between planes bound by van der Waals interactions.

Nanostructured MoO_3 in particular is an attractive material due to its unusual chemistry and electrochromism produced by multiple valence states. Some metal oxides can spontaneously spread over supports forming self-assembled monolayers, which

* Corresponding author.
E-mail addresses: cdiaz@uchile.cl (C. Díaz), colm.odwyer@ul.ie (C. O'Dwyer).

0022-4596/$ - see front matter © 2010 Elsevier Inc. All rights reserved.
doi:10.1016/j.jssc.2010.05.006

has been applied to heterogeneous catalysis [14], but nanostructured MoO_3 can exhibit greater activity, and the possibility of forming stable coordination environments could lead to improved selective oxidation [15] and isomerisation of hydrocarbons, and suitable supported intercalation cathodes. Lamellar or layered α-MoO_3 in its thermodynamically stable orthorhombic form, based on the bilayered arrangement of corner-shared MoO_6 octahedra held together by covalent forces, is also used as an image rotation calibration standard for transmission electron microscopy, but currently only accessible in bulk form with a lamellar structure by tedious synthetic routes.

Despite its importance, success in obtaining nanoscale single-crystal anhydrous MoO_3, compared to other metal oxides, is relatively rare [16,17]. Furthermore, the products are commonly obtained as irregularly agglomerated powders in which the polycrystalline domain size is typically 10–30 nm. Recent reports have shown the nanometer control of sheet thickness for MoO_3 nanobelts and nanoribbons, citing the importance of its properties as a lamellar material [18–20]. Ultimately, the possibility of synthesizing stand-alone micro- and nanocrystals of lamellar α-MoO_3, as both single crystals of micro- and nanoscale sizes in addition to monocrystalline deposits on amorphous and single-crystal surfaces, is a considerable advance. Only localized islands are usually formed on related substrates, making their removal and eventual application quite cumbersome. In addition, the van der Waals bound interatomic spacings are readily available for electrochemical lithium ion storage and release [21].

Our recent reports employing polyphosphazene as solid-state templates for the preparation of metallic nanostructured materials [22] inspired the search for a suitable methodology to produce nanostructured MoO_3 with micro- and nanoscale morphological analogues of its bulk counterpart. This solid-state pyrolysis of organophosphazene/organometallic (SSPO) template method is outlined in Scheme 1. This methodology represents a new synthetic route for the realization of lamellar MoO_3 micro- and nanocrystals with morphologies similar to multi-functional low-dimensional, layered MoO_3.

Although several metallic nanostructured materials can be obtained by other synthetic methods, the relatively long and tedious synthetic procedures are major drawbacks for obtaining the precursors, and generally result in low yields. This is especially true also for the SSPO method using polymers as precursors. Some of these disadvantages are resolved by using organometallic derivatives of cyclophosphazenes as alternative precursors. These organometallic derivatives can be easily prepared by functionalization of $N_3P_3Cl_6$ and subsequent coordination of organometallic fragments [23], giving routinely high yields as either stand-alone crystalline product or as-deposited films. Preliminary results with the trimer $N_3P_3(OC_6H_5)_5(OC_6H_4CH_2CN[Ru])PF_6$ indicate similar results in comparison with the respective polymer [22c].

Here, we report the first successful pyrolysis of the Mo-containing $N_3P_3[OC_6H_4CH_2CN\cdot Mo(CO)_5]_6$ (I) and $N_3P_3[OC_6H_4CH_2CN\cdot Mo(CO)_4\,py]_6$ (II) organometallics, and the characterization of their α-MoO_3 micro- and nanocrystalline products. As will be outlined, pyrolysis of (I) and (II) in air at 800 °C produces crystalline orthorhombic α-MoO_3 single crystals, determined using both electron and ion microscopies in addition to diffraction-based techniques, atomic force microscopy and surface spectroscopies. The size of the crystallites depends on the composition of the precursor and this uniphasic material can be deposited/prepared uniformly on either single-crystal substrates or amorphous supports. The probable mechanism involving the phosphazene as a solid-state template in the formation of MoO_3 is also discussed.

2. Experimental

The precursors (I) and (II) were prepared using a previously reported methodology [23]. Briefly, the trimer $N_3P_3[OC_6H_4CH_2CN]_6$ [23a] and the organometallic compounds $Mo(CO)_5THF$ (generated from UV-irradiation of $Mo(CO)_6$ and THF) and $Mo(CO)_4py_2$ in stoichiometric quantities were stirred in THF and chloroform, respectively. The resulting solids were filtered and washed with an *n*-hexane/ether mixture.

(**I**) 0.5130 g, 1.94 mmol, of $Mo(CO)_6$ in 30 mL methanol was irradiated for 45 min. The yellow solution was transferred to a Schlenk and 0.299 g, 0.32 mmol of $N_3P_3[OC_6H_4CH_2CN]_6$ [23] was added and stirred for 24 h. After this step, the solvent was removed at reduced pressure and the solid washed with diethylether and *n*-hexane. Yield: 0.24 g, 32%. Elem. anal. Calcd for $C_{78}H_{36}N_9O_{36}P_3Mo_6$ (found): C, 40.01 (39.3); H, 1.53 (1.49); N, 5.38 (5.29). ^{1}H NMR (ppm, $CDCl_3$): 7.185 m, 7.01 M, [$-C_6H_4-$]. 1.28s, 2H [$-CH_2-$]. ^{31}P NMR (ppm, acetone-d_6) 8.75 s, ppm. IR(KBr, cm^{-1}): 2963, 2876, 2140 ν(CN), 2065, 1940 ν(CO), 1507, 1485, 1463, 1382, 1268, 1206, 1183, 1165 ν(PN), 957, 886, 850.

(**II**) To $N_3P_3[OC_6H_4CH_2CN]_6$, 0.0506 g, 0.546 mmol in 80 mL chloroform 1.63 mmol $Mo(CO)_4Py_2$, 0.61 g, 1.63 mmol was added also dissolved in the same solvent (40 mL) and stirred at room temperature for 24 h. The solid was then decanted and the

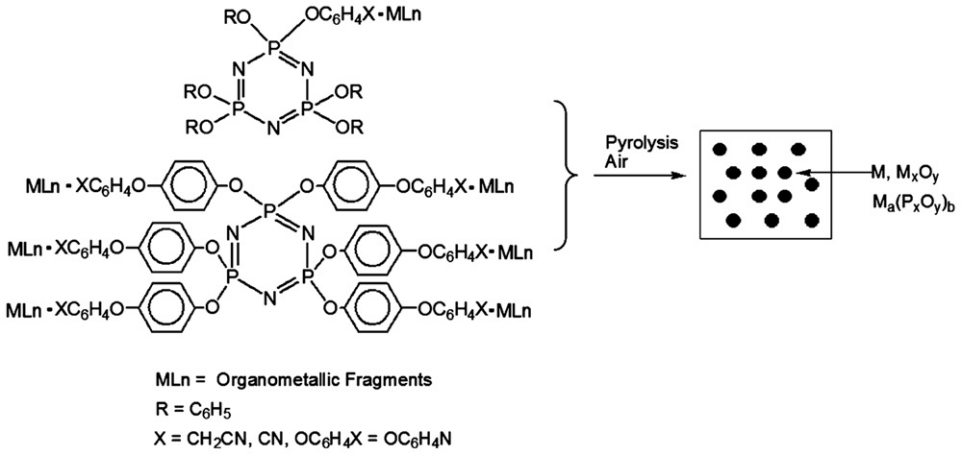

Scheme 1. Schematic representation of the solid-state pyrolysis of organophosphazene/organometallic (SSPO) template method.

supernatant was extracted. The solid was washed twice with chloroform and dried under vacuum. Yield 0.08 g, 63%. Elem. anal. Calcd for $C_{102}H_{60}N_{30}P_3Mo_6$ (found): C, 46.37 (45.5); H, 2.27 (2.3); N, 7.95 (7.85). ^{1}H NMR (ppm, $CDCl_3$): 8.29 m, [C_5H_4N]; 7.2 m, 7.1 m, [-C_6H_4–]. 1.3 s, 2H [–CH_2–]. ^{31}P NMR (ppm, acetone-d_6) 8.93 s. IR(KBr, cm^{-1}): 2948, 2840, 2139 ν(CN), 2065, 1940 ν(CO), 1660, 1638; 1585 ν[CC, C_5H_4N], 1461, 1433, 1394; 1206, 1162 ν(PN), 1029, 896, 842.

2.1. Pyrolysis of the precursors

The pyrolysis experiments were carried out by pouring a weighed portion (0.05–0.15 g) of the organometallic trimer into aluminum oxide boats placed in a tubular furnace (Lindberg/Blue Oven model STF55346C-1) under a flow of either air or nitrogen, heated from 25 to 300 °C and then to 800 °C, and annealed for 2 h. The heating rate was 10 °C min^{-1} under an air/N_2 flow rate of 200 mL min^{-1}.

2.2. Characterization of the pyrolytic products

X-ray diffraction (XRD) was conducted at room temperature on a Siemens D-5000 diffractometer with θ–2θ geometry. The XRD data were collected using Cu-$K\alpha$ radiation (40 kV, 30 mA). Scanning electron microscopy (SEM) and energy dispersive X-ray analysis (EDX) were acquired with a JEOL 5410 SEM with a NORAN Instrument micro-probe transmission microscope. Transmission electron microscopy (TEM) was carried out on a JEOL 2011 TEM operating at 200 kV. The finely powered samples were dispersed in *n*-hexane and dropped on a conventional carbon-coated copper grid and dried under a lamp. Atomic force microscopy (AFM) measurements were performed using a Digital Instruments Nanoscope IIIa and Veeco Enviroscope using both contact and tapping mode scans. Suitable depositions were obtained by dissolving trimers (I) and (II) in dichloromethane, dropping on either an oxidized (400 nm SiO_2) surface or (100) single-crystal silicon surfaces, followed by evaporation of the solvent at room temperature. Subsequent pyrolysis was conducted at 800 °C to remove surface bound water. AFM images were acquired with *in-situ* substrate heating to 110 °C. Optical microscopy imaging was performed using a Zeiss A1 Vario Axioscope. Fourier transform infrared (FTIR) characterization was performed in attenuated total reflection mode using a Perkin-Elmer Spectrum 100 spectrometer. X-ray photoelectron spectroscopy (XPS) was conducted on deposits from (I) and (II) on Si and SiO_2 surfaces in normal emission geometry. A VG CLAM 2 spectrometer with an Al $K\alpha$ X-ray source (1486.6 eV), operating at 250 W, were used several centimeters from the samples. The spectra were normalized to the total electron yield to correct for small differences in sample positions and X-ray source intensities. The resulting spectra were fitted by using a Shirley-type background and symmetric Voigt functions with variable Gauss and Lorentz contributions.

3. Results and discussion

The new compounds (I) and (II) are brown or yellow solids, soluble in common organic solvents. IR spectra of (I) clearly exhibit the presence of the $Mo(CO)_5$ moiety. Absorption at 2056 cm^{-1} and a broad band between 1946 and 1908 cm^{-1}, corresponding to ν(CO) vibrations typical of $M(CO)_5$, were observed [22a]. For (II), the respective ν(CO) vibrations are centered at 1985 cm^{-1} and a weak vibration at 2025 cm^{-1} were also observed. The presence of the phosphazene is clearly indicated by the typical ν(CN) [23] bands: at 2140 cm^{-1} for (I) and at 2139 cm^{-1} for (II) of the ligands, as well as by the 1206, 1183, and 1165 cm^{-1} bands for (I) and 1206, 1162 cm^{-1} for (II) corresponding to the PN) band of the ring [23,24]. In the case of the pyridine complex (II) the emergence of a band at 1638 cm^{-1} typical of coordination of pyridine ligand [22a] was also observed. In addition, NMR spectra corroborate the presence of the ligand, *i.e.* the signals corresponding to the C_6H_4 and CH_2 groups were observed as expected (see Experimental section). The total coordination of the $Mo(CO)_5$ or $Mo(CO)_4$py fragments in the six sites of the phosphazene ring is clearly established by the solitary signal in the ^{31}P NMR spectra of both (I) and (II) [22c].

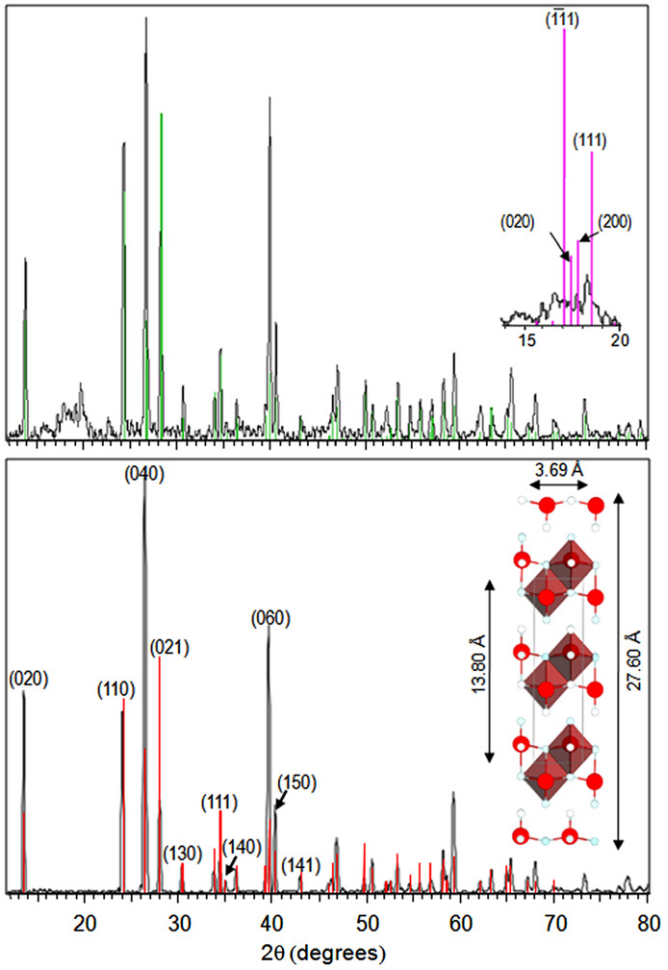

Fig. 1. X-Ray diffraction patterns of the pyrolytic products from (a) (I) and (b) (II). The patterns were indexed to JCPDS 00-001-0706 and JCPDS 00-005-0508 (stick pattern overlaid) for non-hydrated orthorhombic α-MoO_3. The inset to (a) shows the region $14^\circ < 2\theta < 20^\circ$, indexed to monoclinic pyrophosphate (JCPDS 01-072-0880). The inset to (b) shows layered α-MoO_3 unit cell within the repeating crystallographic unit of length $2b = 27.60$ Å.

Pyrolysis of trimers (I) and (II) in air at 800 °C results in a white crystalline solid. The X-ray diffraction (XRD) patterns of the pyrolytic product from (I) and (II), shown in Fig. 1a, b, exhibit excellent correspondence with the standard XRD data for orthorhombic α-MoO_3 (JCPDS 00-005-0508). The pattern in Fig. 1a was taken from large scale pyrolysis of the organometal and shows the pure α-MoO_3 phase in addition to small quantities of residual P_4O_7, which acts as a solid-state stabilizer [22]. The inset to Fig. 1a shows an expanded view of the region $14^\circ < 2\theta < 20^\circ$, indexed to monoclinic pyrophosphate (JCPDS 01-072-0880). The (020), (040) and (060) peaks (see Fig. 1a, b) are predominantly more intense than those from (110), (021), (130),

i.e. (*hk*0) reflections, indicating a two-dimensional growth of the crystallites along the {010} basal planes, as shown schematically by the extended unit cell in Fig. 1b (inset) [2,25]. For the as-obtained pyrolytic product from precursor (II), similar XRD patterns to those for (I) are observed; the relative predominance of the (0*k*0) reflections is more pronounced and the three-dimensional crystal diffraction peaks have a reduced relative intensity. A dominant presence of (*hk*0) would indicate the presence of monoclinic α-MoO_3, but is never observed. Additionally, the presence of metastable β-MoO_3 is not detectable and both precursors are almost entirely orthorhombic α-MoO_3, either as crystalline powder or deposited films.

Both precursors result in micro- and nanoscale crystals exhibiting a high degree of crystallinity; the pronounced (0*k*0) reflection intensities confirm a layered structure packed in the direction of its crystallographic *b*-axis, parallel to the {010} plane as shown in the crystal structure in the inset in Fig. 1b. Within each MoO_6 octahedron, one oxygen atom is essentially unshared, forming a terminal Mo=O bond. The layers themselves are in a staggered arrangement along the *c*-axis and are bound by van der Waals' forces [25] resulting in individual layers of this material forming a turbostratic arrangement. Analysis of the degree of grain orientation and lamellar stacking was determined from XRD data using the Lotgering method [26] using the intensities of (0*k*0) and (*hk*0) reflections for the synthesized samples compared to pure MoO_3. The lamellar orientation degree, *F*, is given by

$$F = \frac{(P-P_0)}{(1-P_0)}; \quad P = \frac{\sum_{0k0} I}{\sum_{hk0} I}$$

where *P* is the ratio of the sums of the (0*k*0) and (*hk*0) reflection intensities, respectively, and P_0 represents similar relative intensities from pure MoO_3. The products from precursor (I) and (II) have lamellar orientation degrees (Lotgering factors) of 0.78 and 0.92, respectively, indicating pronounced turbostratic layering of the products, which are uniphasic, orthorhombic MoO_3 micro- and nanocrystals.

The XRD findings are in agreement with SEM imaging of the products. Fig. 2 clearly shows the typical rectangular morphology of the resulting crystals. Fig. 2a shows the surface of a MoO_3 crystal formed by pyrolysis of (I) on silicon. The surface, as in all samples in this work, is coated with smaller nanocrystals of MoO_3 of similar morphology and crystallinity. Additionally, the EDAX spectrum of all crystallites (from (I) and (II)) exhibited only peaks corresponding to the presence of Mo and O atoms; the spectrum in Fig. 2b is from the large crystal in Fig. 2c where contributions from Au arise from the coating for SEM imaging. The product from precursor (II) is noted to be very similar to that from (I), except that the resulting crystal structures vary in size from micro- to nanocrystals. These pure MoO_3 single crystals are observed with a range of sizes and aspect ratios, all with a characteristic high aspect ratio rectangular morphology. Thus the resulting crystals are distinct and all crystals exhibit identical crystallographic phase and space group and, apart from absolute size and aspect ratio, are self-similar. The shapes of these crystals can be classified into 4 general morphological groups: nano- and microrods, flakes, monoliths and lamina, all of which have length to width aspect ratios typically between 2 and 50. Each of these crystals comprises crystallographically stacked layers of MoO_3, corroborating the XRD findings. Some clear examples of laminar MoO_3 crystals in SEM images are shown in Fig. 2d.

AFM and TEM images were also acquired of individual flakes of the lamellar products from pyrolysis of (I) and (II), and are shown in Fig. 3. After pyrolysis, the crystalline flakes have typical dimensions in the range 200–1000 nm for (I) but 150–300 × 300–700 nm for (II), similar to those in Fig. 2. All flakes are taken from

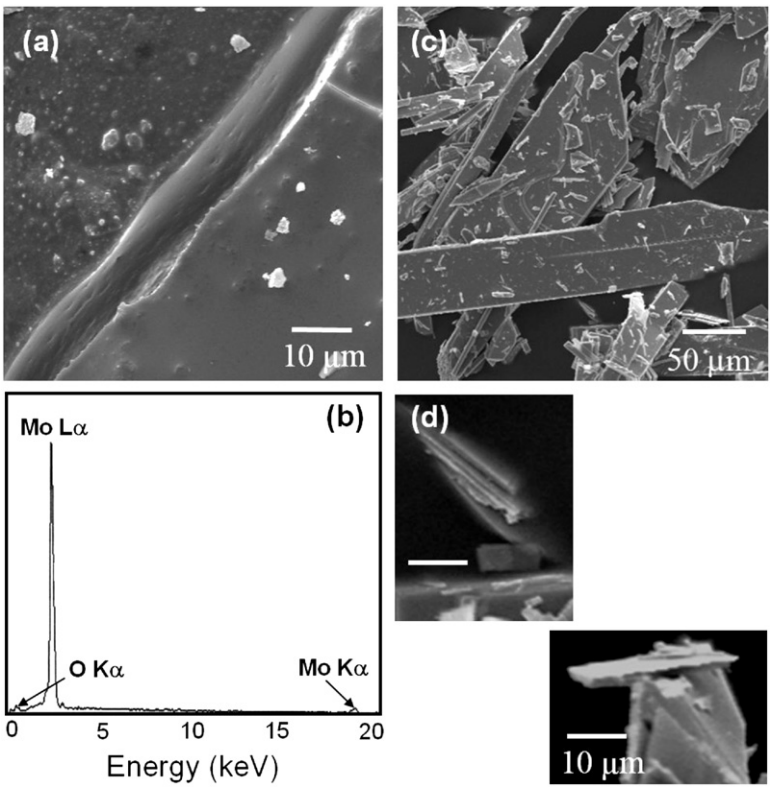

Fig. 2. (a) Scanning electron microscopy images of the pyrolytic products from (I) at beam voltages between 1 and 10 kV. (b) Energy dispersive X-ray analysis of the products showing their bi-elemental (Mo and O) composition. (c) Micro- and nanoscale rods, flakes, monoliths and lamina of MoO_3 obtained after pyrolysis of (II). (d) Individual and stacked lamina of MoO_3 obtained from pyrolysis of (II).

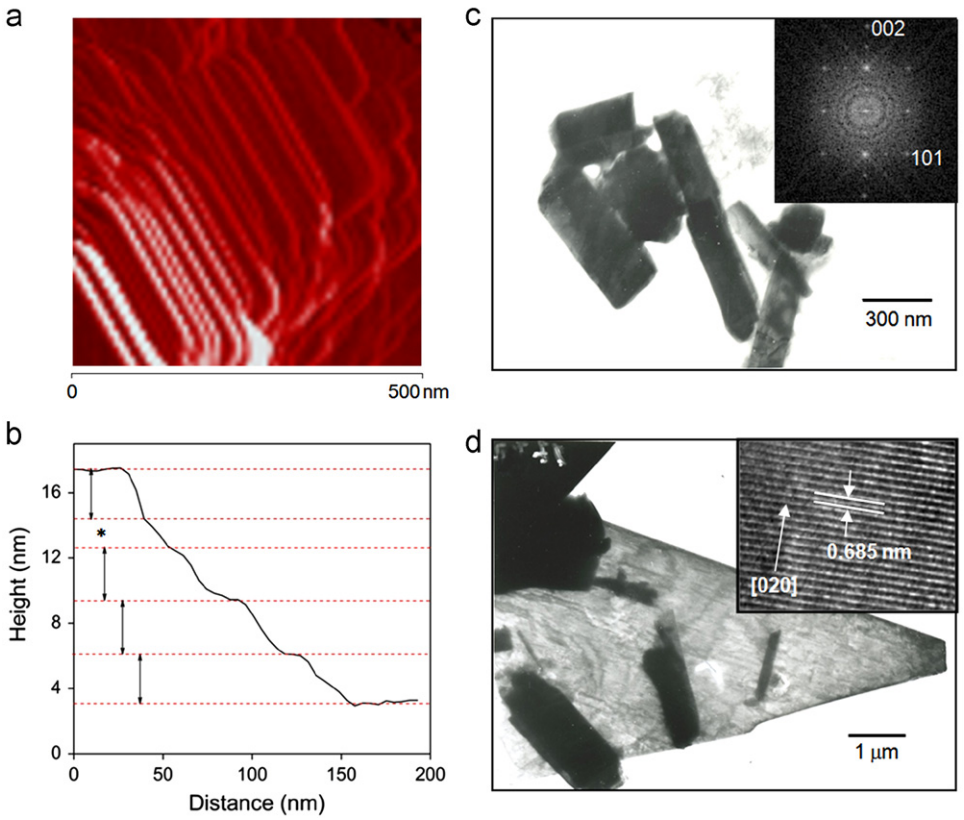

Fig. 3. (a) Contact mode AFM image of crystallographic step features at the edge of a MoO_3 crystal from (I). (b) Line scan profile showing the repeat unit height of 2.7–3.1 nm. The * indicates a step of unusually low thickness. Transmission electron micrographs of the pyrolytic products from (c) (I) and (d) (II) evidencing highly turbostratic flakes and the presence of rod-like lamellar monocrystals of MoO_3. The FFT pattern (inset (c)) taken from HRTEM images acquired along the [010] zone axis confirms single-crystal orthorhombic MoO_3, also evidenced by the HRTEM image inset to (d).

two sources: the surfaces of larger crystals and also from film deposits on Si by mechanical exfoliation. Kalantar-zadeh et al. [20] have suggested that the mechanical exfoliation of MoO_3 sheets delaminates at their weakest bond points, where they are held together by weak van der Waals forces. Microscale thickness flakes exhibited characteristic layering at their edges, as shown in the high resolution contact AFM image in Fig. 3a. The surface profile shown in Fig. 3b exhibits typical layering, where the repeat step height is consistently in the range 2.7–3.1 nm. This value is close to twice the magnitude of b lattice parameter for α-MoO_3 ($b=1.38$ nm) based on the structure depicted in Fig. 1b. In some cases, step heights of roughly half this value (similar to b) are observed (see * in Fig. 3b), but is not a common observation.

TEM analysis in Fig. 3c and d shows the individual crystals and also the exfoliated flakes. The corresponding electron diffraction patterns and FFT can be indexed to non-hydrated orthorhombic MoO_3 with reconstructed lattice parameters of $a_0=0.395$ nm, $b_0=1.383$ nm, $c_0=0.369$ nm; space group: *Pnma*. The HRTEM image in Fig. 3d acquired perpendicular to the growth direction shows MoO_3 lattice fringes spaced by 0.685 nm, corresponding to the spacing between the (020) planes. The flakes for TEM measurement actually have thicknesses of the order of 2–6 molecular layers of MoO_3 with excellent layer matching. Predominant intensity (020) reflections are observed typical of lamellar (010) stacking along the c-axis, in agreement with indications of lamellar two-dimensional growth from XRD data. The crystalline structures obtained as product from precursor (II) are routinely observed to be larger in length and width than from (I), according to the SEM and TEM data, and correspondingly, exhibit higher relative (0k0) reflections in their XRD spectra (Fig. 1b). The planar or lamellar topology of these turbostratic orthorhombic crystals, which consist of bilayers parallel to the (010) plane weakly bound by covalent interactions, would allow exfoliation of nanoscale flake crystals from microscale single-crystal structures, which is what is usually observed experimentally.

In order to apply these nanostructured lamellar materials to surfaces or supports, synthesis and subsequent pyrolysis on suitable substrates was carried out to characterize the as-deposited morphology and investigate the mechanism of surface spreading and long-range uniformity in crystallinity and coverage/thickness. Suitable depositions were obtained by dissolving trimers (I) and (II) in dichloromethane, dropping on either an oxidized (400 nm SiO_2) surface or (100) single-crystal silicon surfaces, followed by evaporation of the solvent at room temperature. Subsequent pyrolysis was conducted at 800 °C. Surprisingly few AFM studies of MoO_3 have been reported in the literature [4,16] for uniform MoO_3 deposition on surfaces directly and this is the first report of single-crystal deposition of this material on monocrystalline and amorphous surfaces. Scanning probe and scanning tunneling microscopy (SPM and STM) techniques have been principally used for the atomic scale study of MoO_3 island growth on both Au{111} and MoS_2 along with the friction-reducing benefits of a Mo/MoS_2/MoO_3/MoS_2 sandwich layer system [4]. Atomic force microscopy (AFM) imaging of pyrolyzed substrates, shown in Fig. 4, reveals a surface morphological dependence of the coverage on the composition of the precursor: from (I) craters of typically 10–20 nm in depth and two principal diameters of either ~500 nm or ~60–100 nm are routinely observed (Fig. 4a–c) whereas from (II) encrustations or islands of 23–50 nm in height and diameters of 0.6–1.2 μm are

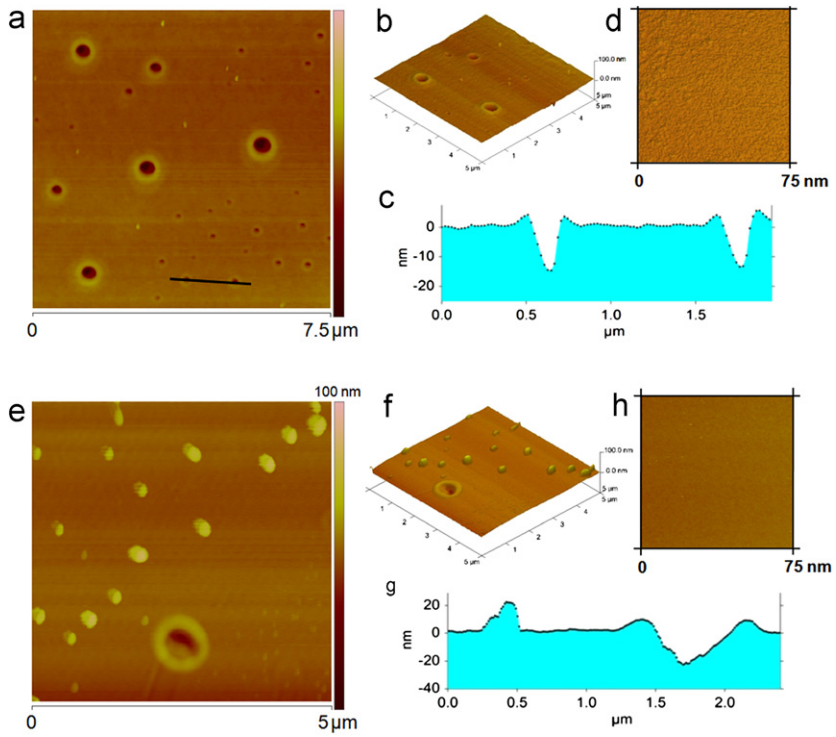

Fig. 4. Atomic force microscopy images of the products from (a–d) (I) and (e–h) (II) pyrolyzed on a silicon substrate. High resolution images from (I) in (d) and from (II) in (h) show very smooth surfaces. The corresponding line scans highlight the typical feature dimensions resulting from spreading during pyrolysis.

formed (Fig. 4e–g), on surfaces that are otherwise covered with a relatively uniform layer of MoO_3 with rms roughness values of 2.6–4 nm for both surfaces over 100 μm^2 (including the surface features). High resolution contact AFM images shown for precursor (I) in Fig. 4d and precursor (II) in Fig. 4h show that the deposition using precursor (II) results in an extremely smooth surface. This is also the deposition that gives the lowest density of crater formation, but also a higher density of excess MoO_3 in the form of islands on the surface. Although both islands and craters are found on the surface deposits from both precursors, the general trend is a predominance of craters from (I) and islands of MoO_3 from pyrolysis of (II) whether deposited on Si or SiO_2. As the pyrolysis was conducted in air, the presence of O_2 promotes the spreading of MoO_3 [27].

The formation of islands and craters in pyrolyzed precursor functionalized surfaces is reminiscent of the ramified-cluster-diffusion mechanism [16,28], which can explain the process of spreading on the nanoscale in most studies thus far, *i.e.* bulk MoO_3 spread in a ramified manner in the form of agglomerated cluster islands. The overall uniformity of the deposit (from either precursor) depends on the nature of that precursor and the mechanism of pyrolysis. Investigation of the surface by optical microscopy was also performed over larger deposition areas. Deposits on SiO_2 were examined since the large refractive index contrast afforded by the SiO_2 allows imaging of very thin several-molecule-thick layers in a similar manner to optical microscopy of graphene [29]. Fig. 5a shows the typical MoO_3 film deposition prior to full coverage. The red regions are MoO_3 and the deposit is interspersed with craters. The blue colour comes from the SiO_2 under white light. The boxed region in Fig. 5a shows how the quantity or thickness of MoO_3 varies along the surface. In this case, it is always observed that the higher the density of craters, the lower the film thickness in accord with a cluster diffusion spreading of a finite local amount of product. For greater quantities of precursor, we observe the same type of film coverage as was seen by AFM in Fig. 4e, *i.e.* a uniform deposit with some evidence for cratering (but the craters do not extend down to the SiO_2 layer) and the presence of MoO_3 islands (shown in red). The contrast is less effective in Fig. 5b compared to Fig. 5a due solely to the reduced depth of the craters. Since the deposit can transfer to the Si or SiO_2 in single-crystal form, optical imaging of individual and several monolayers was possible. Fig. 5c shows an optical micrograph of the coated SiO_2 surface, a further single layer on top of this, marked by (1), and also a double layer (2), which appears as the brightest, green region. Similar to Fig. 3 for single crystals, the surface deposit is also layered which was confirmed by AFM.

As with polyphosphazenes [22,23], insight into the possible mechanism of the pyrolysis was obtained from thermogravimetric analysis and differential scanning calorimetric (TGA/DSC) studies obtained during the pyrolysis of precursors (I) and (II) in both air and nitrogen atmospheres, which are shown in Fig. 6. The deposits were heated at a rate of 10 °C min^{-1} from ambient (25–800 °C under a constant air flow of 200 mL min^{-1}). Conditions similar to those of the preparative pyrolysis experiments were used. From samples of precursor (I), the TGA curves shown in Fig. 6a (in air and nitrogen) indicate a gradual loss of CO_2 and H_2O from 150 to 350 °C, which corresponds to oxidation of the carbon atoms of the organic matter. The data indicate that the complete oxidation of carbon is much more efficient in air, even though under N_2 significant oxidation of carbon as CO_2 and H_2O still does occur. This is crucial for ensuring a pristine MoO_3 surface during pyrolysis, for example, and not routinely found by other general approaches [30]. This agrees with the intense exothermic peaks in the DSC response shown in Fig. 6b, at 284 and 494 °C, which are normally observed after combustion of the organic part of organometallic compounds [31,32] and crystallization of the MoO_3, which is also represented schematically in Fig. 6c.

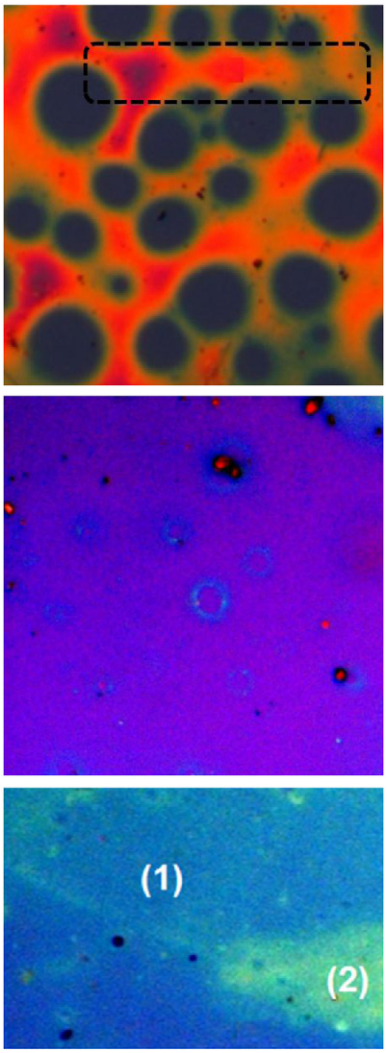

Fig. 5. Optical microscopy of MoO_3 films at (a) low quantity coverage where cratering of the deposit is observed (b) smooth deposition for thicker deposits and (c) several monolayer thick lamina. In (a), the blue regions in craters come from the SiO_2 under white light, the red regions from MoO_3. Variations in MoO_3 thickness are shown in the boxed region. In (b) the red crystals are MoO_3. In (c) single and double layer MoO_3 lamina are marked (1) and (2), respectively. (For interpretation of the references to colour in this figure legend, the reader is referred to the web version of this article.)

This loss of the organic matter produces vacancies in the previously formed cyclomatrix, which allows agglomeration of the metallic particles followed by growth of the nanoclustered structures. The organometallic fragments $Mo(CO)_5$ and $Mo(CO)_4$py linked to the phosphazene precursors (I) and (II), respectively, as determined from previous studies [33], lose carbon monoxide upon heating leading to Mo centers that migrate toward the vacancies generated in the cyclomatrix. Similarly, the phosphazenic phosphorus and the nitrogen polymeric chain evolve as the respective oxides upon oxidation, and do so as single crystals. As noted during the pyrolysis of organometallic derivatives of polyphosphazenes, the remaining phosphorus oxide, as shown by XRD, acts as a structural stabilizer.

Infrared vibrational and X-ray photoelectron spectroscopies were also conducted on few-monolayer coverage MoO_3 deposits after pyrolysis of (II). The FTIR spectrum in Fig. 7a exhibits three distinct vibrations. The secondary electron image from a focused Ga^+ beam is shown in Fig. 7b and the corresponding AFM image in Fig. 7c. The bridging Mo–O–Mo stretching vibration observed at 809 cm^{-1} is characteristic of most molybdenum oxides, where the stoichiometric ratio of oxygen is reduced, *e.g.* for Mo^{4+} as MoO_2 and Mo^{6+} as MoO_3. The α-Mo–O vibration at 855 cm^{-1} is distinctly related to α-MoO_3, which is most typically found in several crystal structures. Corroboration of the orthorhombic structure deduced from diffraction measurements is found with the observation of the terminal molybdyl bond vibration (M=O) measured at 981 cm^{-1}; this stretching vibration is unique to α-MoO_3 in an orthorhombic structure. In contrast to the Mo–O–Mo and M=O vibrations, the α-Mo–O vibrations are comparatively broad band. This is most likely linked to the varied terminal surface morphology from various crystal facets, since FIB and AFM imaging indicate sub-nanoscale features on the most pristine (smoothest) regions of deposit.

XPS measurements conducted at various take-off angles conclude that the deposited layers (and uppermost atomic layers) are pure MoO_3, since the wavenumber limit of the FTIR spectrometer prevented determination of true lattice vibrational modes, rather the IR active stretching modes. The Mo 3*d*, Mo 3*p*, O 1*s* and C 1*s* core-level peaks are shown in Fig. 8a–d, respectively. The Mo $3d_{5/2}$ and Mo $3d_{3/2}$ doublet shown in Fig. 8a are observed at binding energies of 232.5 and 235.6 eV, respectively, with the corresponding Mo $3p_{3/2}$ and Mo $3p_{1/2}$ measured at 399.2 and 416.6 eV (Fig. 8b). These doublets are consistent with Mo only in its hexavalent(VI) oxidation state as MoO_3. For all samples studied from (I) or (II) on Si or SiO_2, deconvolution of the spectra showed there was no appreciable shift in binding energy of Mo 3*d* core-level emission towards lower energy, confirming the complete stoichiometry of the product, *i.e.* we never observe sub-stoichiometric molybdenum oxides. The O 1*s* peak, for pyrolytic products from (I) and (II), is observed only at 530.8 eV with no dominant overlapping contributions from other oxygen species [34]. Examination of the C 1*s* core-level spectrum confirms that there are no C–O bonds and that the detected carbon is adventitious. Quantification of the O 1*s* core-level spectrum in α-MoO_3 formed by other methods often includes contributions from two other species of O. The presence of OH groups would give a shoulder peak at 531.8 eV (scaled to the data presented here) and another at 532.7 eV, associated with adsorbed water [35]. The shoulder peak in the deconvoluted O 1*s* spectrum in Fig. 8c corresponds to adsorbed moisture, most probably from exposure to air prior to chamber loading as no indicative vibrations from hydrated $MoO_3 \cdot nH_2O$ are observed in the IR data. Thus, dedicated surface studies of the deposited product confirms a self-similar crystal structure to the individual crystals formed during pyrolysis of the organometallic Mo-containing derivatives of cyclotriphosphazenes directly. This readily accessible technique is promising for the synthesis of important lamellar materials and their incorporation onto surfaces and supports.

4. Conclusions

The pyrolysis of organometallic Mo-containing derivatives of cyclotriphosphazenes is found to be a simple, versatile and useful method to grow monocrystalline α-MoO_3. The products can be micro- and nanocrystals with a high degree of phase purity and laminarity, and also smooth, single-crystal deposits (monolayers and thin films) of α-MoO_3 on crystalline silicon and amorphous silicon dioxide surfaces by cluster diffusion during pyrolysis. The size and the morphology can be tailored by compositional control of the organometallic precursor for a given surface. Transmission electron microscopy and electron diffraction measurements confirm the nanoscale crystallinity observed in larger deposits

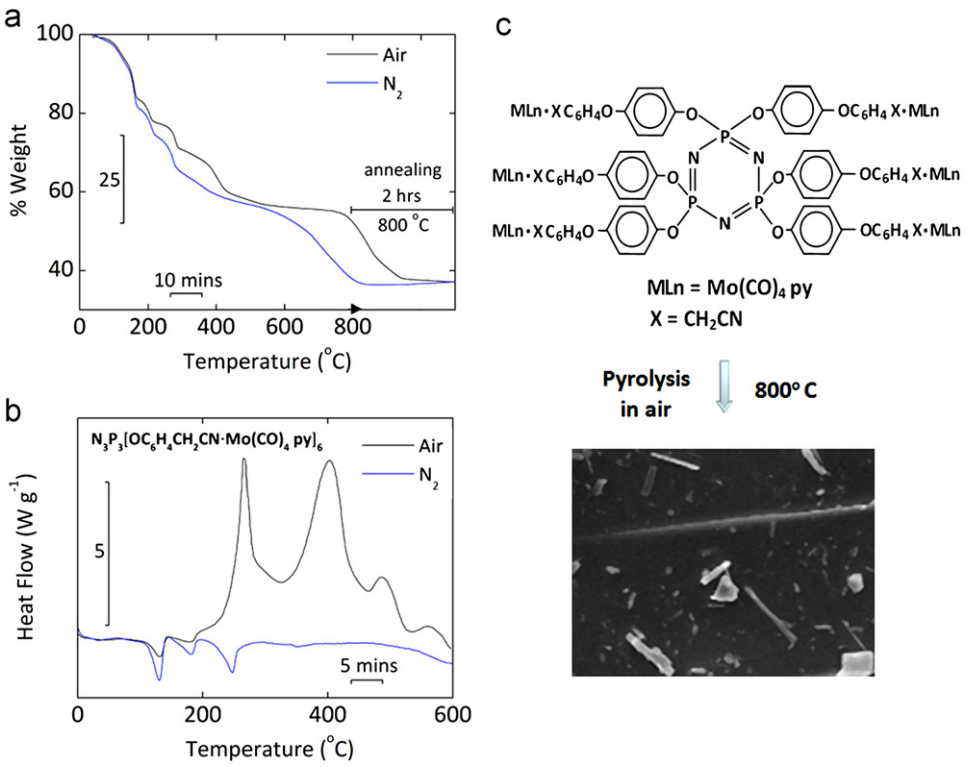

Fig. 6. (a) Differential scanning calorimetric analysis of the pyrolysis of the product from (I) in air and N_2. Pyrolysis in air exhibits intense exothermic peaks during organic combustion. Total weight = 4.000 mg. (b) Thermogravimetric analysis of the pyrolytic product from (I); 100% = 9.000 mg. (c) Pyrolysis condition and schematic of organometallic metal carbonyl to yield single-crystal MoO_3.

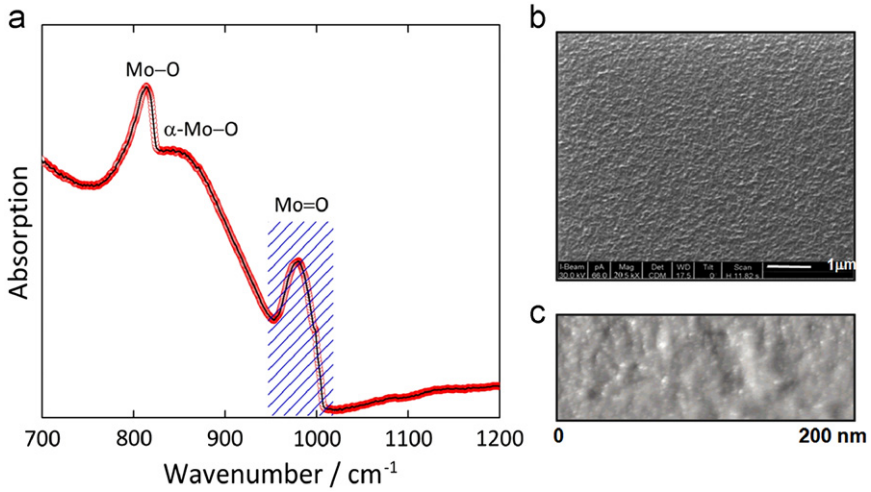

Fig. 7. (a) Fourier transform infrared spectroscopy (absorption) of the pyrolytic product from (I) deposited on (100) silicon. The spectrum evidences the terminal molybdyl (M=O) vibration characteristic of orthorhombic α-MoO_3 and this is highlighted by the hatched region. (b) Secondary electron image from a focused Ga^+ beam scan of the morphology of the deposited product after pyrolysis. (c) AFM image of the surface morphology of the post-pyrolytic product of (I) acquired in contact mode in vacuum after *in-situ* heating to 110 °C to remove surface bound water.

by XRD where the laminar single crystals are orthorhombic α-MoO_3. The same crystalline phase is found for layer deposits on either silicon or silicon dioxide after pyrolysis. AFM and ion-beam morphology measurements indicate a smooth film deposit for which IR and XPS analysis confirm stoichiometric MoO_3 and successful combustion of the organic matter from the precursor.

The technique is shown to be effective in realizing stand-alone micro- and nanostructures of an important electrochromic and intercalation host material (MoO_3), but can also be directly applied to the formation of other valve and transition metals, leading to a variety of micro- and nanostructured materials and their oxides through a very clean and quick synthetic methodology involving pyrolysis of metal-carbonyl derivatives.

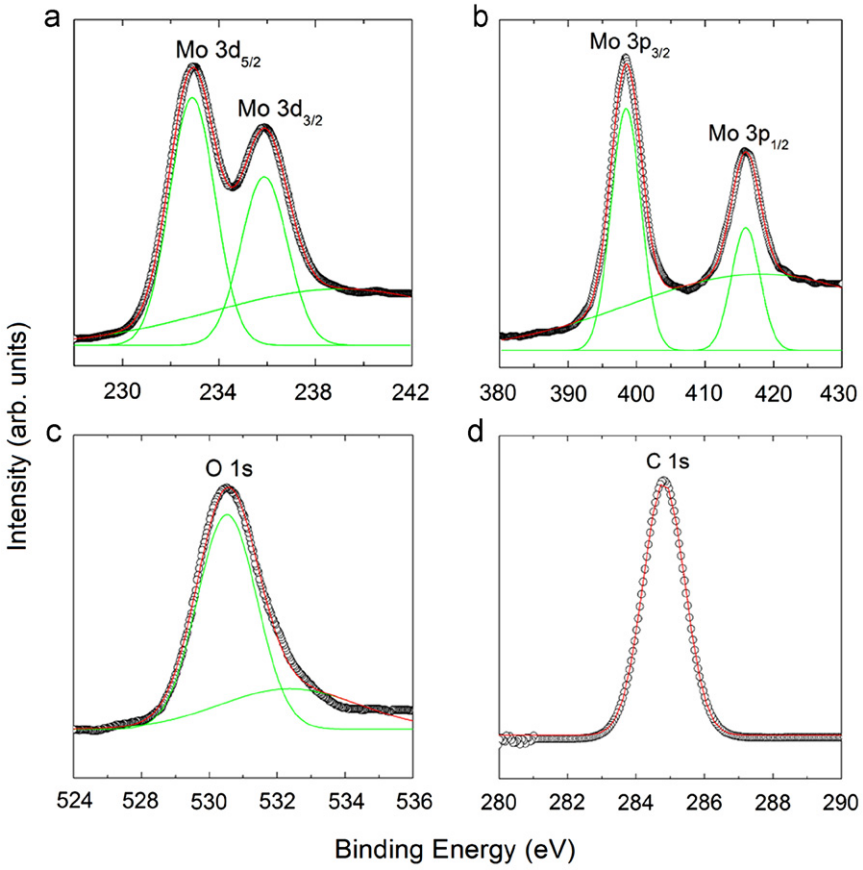

Fig. 8. High resolution XPS spectra acquired from the deposit in Fig. 7 showing (a) the Mo 3*d* core-level doublet (b) Mo 3*p* doublet peaks (c) the O 1*s* photoelectron emission and (d) the C 1*s* binding energy.

Acknowledgments

Financial support from FONDECYT Grant nos. 1085011, 1095135, 1090683, and 1090282 is acknowledged. V.L. acknowledges PBCT Grant ACT027. Part of this work was conducted under the framework of the INSPIRE programme, funded by the Irish Government's Programme for Research in Third Level Institutions, Cycle 4, National Development Plan 2007–2013.

References

[1] M. Greenblatt, Chem. Rev. 88 (1988) 31.
[2] J.N. Yao, K. Hashimoto, A. Fujishima, Nature 355 (1992) 624.
[3] H.C. Zeng, Inorg. Chem. 37 (1998) 1967.
[4] S. Kamiya, D. Tsuda, K. Miura, N. Sasaki, Wear 257 (2004) 1133.
[5] H.M. Kim, T. Fukomoto, S. Hayashi, K. Yamamoto, J. Phys. Soc. Jpn. 63 (1994) 2194.
[6] R. Chevrel, M. Hirrien, M. Sergent, Polyhedron 5 (1986) 87.
[7] T. Caillat, J.P. Fleurial, G.L. Snyder, Solid State Sci. 1 (1999) 535.
[8] N.A. Chernova, M. Roppolo, A.C. Dillon, M.S. Whittingham, J. Mater. Chem. 19 (2009) 2526.
[9] V. Hornebecq, Y. Mastai, M. Antonietti, S. Polarz, Chem. Mater. 15 (2003) 3586.
[10] P. Poizot, S. Laruelle, S. Grugeon, L. Dupont, J.M. Tarascon, Nature 407 (2000) 6803.
[11] T. Brezesinski, J. Wang, S.H. Tolbert, B. Dunn, Nat. Mater. 9 (2010) 146.
[12] P.L. Taberna, S. Mitra, P. Poizot, P. Simon, J.-M. Tarascon, Nat. Mater. 5 (2006) 568.
[13] S. Hu, X.J. Wang, Am. Chem. Soc. 130 (2008) 8126;
C. O'Dwyer, V. Lavayen, D.A. Tanner, S.B. Newcomb, E. Benavente, G. Gonzalez, C.M. Sotomayor Torres, Adv. Funct. Mater. 19 (2009) 1736.
[14] [a] F.-S. Xiao, S. Zheng, J. Sun, R. Yu, S. Qiu, R. Xu, J. Catal. 176 (1998) 474;
[b] Z. Li, L. Gao, S. Zheng, Appl. Catal., A: Gen. 236 (2002) 163.
[15] M. Goto, in: K. Tanabe, Y. Seitama, K. Fueki (Eds.), Metal Oxides and Composite OxidesKodansha, Tokyo, Japan, 1991, p. 186.
[16] [a] J. Wang, K.C. Rose, C.M. Lieber, J. Phys. Chem. B 103 (1999) 8405;
[b] Z. Song, T. Cai, Z. Chang, G.L.A. Rodriguez, J. Hrbek, J. Am. Chem. Soc. 125 (2003) 8059.
[17] S. Li, I.N. Germanenko, M.S. El-Shall, J. Clust. Sci. 10 (1999) 533.
[18] S. Wang, Y. Zhang, X. Ma, W. Wang, X. Li, Z. Zhang, Y. Qian, Solid State Commun. 136 (2005) 283.
[19] T. Siciliano, A. Tepore, E. Filippo, G. Micocci, M. Tepore, Mater. Chem. Phys. 114 (2009) 687.
[20] K. Kalantar-zadeh, J. Tang, M. Wang, K.L. Wang, A. Shailos, K. Galatsis, R. Kojima, V. Strong, A. Lech, W. Wlodarski, R.B. Kaner, Nanoscale 2 (2010) 429.
[21] D. Mariotti, H. Lindström, A. Chandra Bose, K. Ostrikov, Nanotechnology 19 (2008) 495302.
[22] [a] C. Díaz, M.L. Valenzuela, Macromolecules 39 (2006) 103;
[b] C. Díaz, M.L. Valenzuela, S. Ushak, V. Lavayen, C. O'Dwyer, J. Nanosci. Nanotechnol. 9 (2009) 1825;
[c] C. Díaz, M.L. Valenzuela, D. Bravo, V. Lavayen, C. O'Dwyer, Inorg. Chem. 47 (2008) 11561.
[23] [a] C. Díaz, M. Barbosa, Z. Godoy, Polyhedron 23 (2004) 1027;
[b] C. Díaz, I. Izquierdo, F. Mendizábal, N. Yutronic, Inorg. Chim. Acta 294 (1999) 207.
[24] D.M. Adams, in: Metal–Ligand and Related Vibrations: A Critical Survey of the Infrared and Raman Spectra of Metallic and Organometallic CompoundsSt. Martin's Press, New York, 1967.
[25] [a] V. Sánchez, E. Benavente, V. Lavayen, C. O'Dwyer, C.M. Sotomayor Torres, G. González, M.A. Santa Ana, Appl. Surf. Sci. 252 (2006) 7941;
[b] C. O'Dwyer, V. Lavayen, D. Fuenzalida, H. Lozano, E. Benavente, M.A. Santa Ana, G. González, C.M. Sotomayor Torres, Small 4 (2008) 990.
[26] F.K. Lotgering, J. Inorg. Nucl. Chem. 9 (1959) 357.
[27] G. Mestl, N.F.D. Verbruggen, F.C. Lange, B. Tesche, H. Knözinger, Langmuir 12 (1996) 1817.
[28] H. Knöziger, E. Taglauer, Catalysis, vol. 10, The Royal Society of Chemistry, Cambridge, UK, 1993, p. 1.
[29] K.S. Novoselov, D. Jiang, F. Schedin, T.J. Booth, V.V. Khotkevich, S.V. Morozov, A.K. Geim, Proc. Natl. Acad. Sci. USA 102 (2005) 10451.
[30] A. Datta, J.R. Regalbuto, C.W. Allen, Ultramicroscopy 29 (1989) 233.
[31] E.R. Laite, N.L. Carreño, E. Longo, F.M. Pontes, A. Barison, A.G. Ferreira, Y. Maniette, Y.A.G. Varela, Chem. Mater. 14 (2002) 36.
[32] B.C. Tappan, M.H. Huynh, M.A. Hiskey, D.E. Chavez, E.P. Luther, J.T. Mang, S.F. Son, J. Am. Chem. Soc. 128 (2006) 6589.
[33] [a] G. Carriedo, F.J. García Alonso, C. Díaz, M.L. Valenzuela, Polyhedron 25 (2006) 105;
[b] I.M. Watson, J.A. Connor, R. Whyman, Polyhedron 8 (1989) 1794.
[34] T.L. Barr, J. Phys. Chem. 82 (1978) 1801.
[35] J. Torres, J.E. Alfonso, L.D. López-Carreño, Phys. Stat. Sol. (c) 2 (2005) 3726.